J. Fluid Mech. (2020), *vol*. 906, A1.
Published by Cambridge University Press

doi:10.1017/jfm.2020.746

Reducing aerofoil–turbulence interaction noise through chordwise-varying porosity

Lorna J. Ayton[1],†, Matthew J. Colbrook[1],†, Thomas F. Geyer[2], Paruchuri Chaitanya[3] and Ennes Sarradj[4]

[1]Department of Applied Mathematics and Theoretical Physics, University of Cambridge, Cambridge CB3 0WA, UK

[2]Brandenburg University of Technology, Cottbus-Senftenberg, 03046, Cottbus, Germany

[3]Faculty of Engineering and the Environment, University of Southampton, Burgess Road, Southampton SO16 7QF, UK

[4]Technical University Berlin, Department of Technical Acoustics, Einsteinufer 25, D-10587, Berlin, Germany

(Received 6 May 2020; revised 24 August 2020; accepted 3 September 2020)

This paper considers the effects of smoothly varying chordwise porosity of a finite perforated plate on turbulence–aerofoil interaction noise. The aeroacoustic model is made possible through the use of a novel Mathieu function collocation method, rather than a traditional Wiener–Hopf approach which would be unable to deal with chordwise-varying quantities. The main focus is on two bio-inspired porosity distributions, modelled from air flow resistance data obtained from the wings of barn owls (*tyto alba*) and common buzzards (*buteo buteo*). Trailing-edge noise is much reduced for the owl-like distribution, but, perhaps surprisingly, so too is leading-edge noise, despite both wings having similar porosity values at the leading edge. A general monotonic variation is then considered indicating that there may indeed be a significant acoustic impact of how the porosity is distributed along the whole chord of the plate, not just its values at the scattering edges. Through this investigation, it is found that a plate whose porosity continuously decreases from the trailing edge to a zero-porosity leading edge can, in fact, generate lower levels of trailing-edge noise than a plate whose porosity remains constant at the trailing-edge value.

Key words: noise control

1. Introduction

The use of porosity as an adaptation to traditional rigid impermeable aerofoils is a commonplace area of interest for minimising aerofoil–turbulence interaction noise (Geyer, Sarradj & Giesler 2012; Roger, Schram & De Santana 2013; Ayton 2016; Chaitanya *et al.* 2020). Both leading-edge noise, generated by upstream turbulence impinging on the aerofoil, and trailing-edge noise (also known as self-noise), generated by boundary layer

† Email addresses for correspondence: l.j.ayton@damtp.cam.ac.uk, m.colbrook@damtp.cam.ac.uk

turbulence scattering off the trailing edge can be reduced by replacing an impermeable aerofoil with a fully porous aerofoil (Geyer, Sarradj & Fritzsche 2010), or partially porous aerofoil (Geyer & Sarradj 2019).

To date, these investigations, theoretical (Ayton 2016), numerical (Cavalieri, Wolf & Jaworski 2016; Bae & Moon 2011) and experimental (Geyer *et al.* 2010; Geyer & Sarradj 2019), focus on using one uniform material to impose the porosity, with chordwise variations achieved only through the use of partially porous aerofoils wherein there is an unavoidable and instantaneous variation of the boundary from impermeable to permeable. At this junction, additional noise is generated by edge scattering (Rienstra & Peake 2005; Ayton 2016). However, the benefit of a partially porous aerofoil is in its aerodynamics rather than its acoustics; fully porous aerofoils, whilst acoustically beneficial, have significant aerodynamic penalties (Geyer *et al.* 2010); on the other hand, partially porous aerofoils have lessened aerodynamic penalties but produce more noise than fully porous aerofoils (Iosilevskii 2011; Geyer & Sarradj 2019). The steady aerodynamics of partially porous aerofoils have previously been predicted theoretically by Iosilevskii (2011), which has been extended to aerofoils with porosity gradients by Hajian & Jaworski (2017).

This paper, therefore, investigates the effect of porosity gradients on the noise generated by aerofoil–turbulence interaction. We also implement the Riemann–Hilbert solution of Hajian & Jaworski (2017) to determine the lift coefficient, and thus a measure of the aerodynamic performance of the plates. In these models we allow an arbitrary variation in porosity along a finite perforated flat plate, modelling a thin permeable aerofoil.

The acoustic response will be achieved through a Mathieu collocation method (Colbrook & Priddin 2020). This method restricts us to solving for the acoustics in zero-lift configurations (zero angle of attack in uniform mean flow). The combined aeroacoustic and aerodynamic results will, therefore, indicate the qualitative trends of performance as we vary the porosity along the plate although, since the acoustics are restricted to the zero-lift configuration, they will not be quantitatively comparable.

Throughout this paper, we pay particular attention to monotonic porosity distributions as inspired by two species of birds: barn owls (*tyto alba*), known for their silent flight (Graham 1934; Lilley 1998), and common buzzards (*buteo buteo*). We recreate these chordwise-varying porosity distributions in our flat-plate model as an initial study into the effects of porosity distributions on both aerofoil–turbulence interaction noise and potential lift, before considering more general monotonic distributions. Porosity is a known feature that promotes the silent flight of owls. Therefore, we expect the owl-like distribution to outperform the buzzard-like distribution acoustically, although we note there are many other features we do not consider in our model, such as serrations and canopies (Jaworski & Peake 2020), which aid the owl's silent flight. We also note these two species have different flight speeds; the owl flies at speeds 6–10 ms^{-1} (Neuhaus, Bretting & Schweizer 1973) and the buzzard at a mean speed of 11.6 ms^{-1} (Alerstam *et al.* 2007). Mean flow is accounted for in our model, but we apply a low Mach number approximation throughout which, particularly for trailing-edge noise, eliminates the difference in flight speed.

The layout of this paper is as follows. In § 2, we discuss the set-up of the acoustic mathematical model and the Mathieu collocation method for solving the acoustic problem. In § 3, we review the aerodynamic model from Hajian & Jaworski (2017), which we shall use to calculate lift coefficients. In § 4, we discuss the measurements taken from birds' wings and how we relate these to the mathematical model of porosity on a flat plate. In § 5, we present results and discuss general monotonic porosity variations. Finally, our conclusions are given in § 6.

2. Mathematical model for the acoustics

We consider an incident field impinging on a flat plate situated at $-1 \leq x \leq 1$ and $y = 0$, where lengths have been non-dimensionalised by semi-chord. The plate is in uniform horizontal flow, with velocities non-dimensionalised by the far-upstream mean flow velocity. The incident field will have velocity potential denoted by ϕ_I and the scattered field by ϕ. The incident pressure field is given by $p_I = -\rho_f(\mathrm{D}\phi/\mathrm{D}t)$, where ρ_f is the mean fluid density and $\mathrm{D}\phi/\mathrm{D}t$ denotes the material derivative. Pressure shall henceforth be non-dimensionalised by $\rho_f c_0^2$ with c_0 denoting the speed of sound, so that throughout we deal with dimensionless fields ϕ_I and ϕ.

We assume that ϕ has the usual time dependence $\mathrm{e}^{-\mathrm{i}\omega t}$ (which will be omitted throughout), and hence for low Mach number flow, ϕ satisfies the Helmholtz equation

$$\left(\frac{\partial^2}{\partial x^2} + \frac{\partial^2}{\partial y^2} + k_0^2\right)\phi = 0, \tag{2.1}$$

where $k_0 = \omega/c_0$ is the acoustic wavenumber for angular frequency ω.

We apply an impedance boundary condition given by

$$\frac{\partial \phi}{\partial y} + \frac{\partial \phi_I}{\partial y} = \mu(x)\,(\phi_u - \phi_l) = \mu(x)[\phi](x), \tag{2.2}$$

to model the effects of the porous plate, where $\mu = \alpha_H K_R/(\pi r^2)$ is the porosity parameter (Howe, Scott & Sipcic 1996; Jaworski & Peake 2013). Here K_R is the Rayleigh conductivity (Rayleigh 1945), which for evenly spaced circular apertures of radius r, is given by $K_R = 2r$. The fractional open area is α_H (Howe 1998). Such a model is valid for $\alpha_H^2 \ll 1$, and $k_0 r \ll 1$. We use the notation ϕ_u and ϕ_l to denote the values of the field just above and just below the plate respectively, and the jump in ϕ across the plate is denoted by $[\phi]$. Finally, the scattered field is required to satisfy the Sommerfeld radiation condition for outgoing waves at infinity.

Note that, unlike previous theoretical models (Jaworski & Peake 2013; Ayton 2016), we allow the porosity parameter $\mu(x)$ to vary along the plate. This could be achieved in a number of practical ways; we could link its variation to a variation in α_H, keeping r and K_R constant along the plate. Thus the number of apertures in the plate per unit area varies along the chord, but the size of the apertures remains constant. An identical porosity distribution, i.e. an identical variable $\mu(x)$, could alternatively be achieved through variation of the aperture radius, or a combination of both varying radius and open area. Any such variation presents itself in our model as a fundamental variation in acoustic impedance, governed by the single parameter $\mu(x)$. A specification of how one practically implements the variation of impedance is not required. Nevertheless, throughout this paper, for simplicity, we shall describe the porosity (impedance) distribution as arising due to variation of aperture spacing, α_H, rather than a full variation of $\alpha_H K_R/r^2$. This, therefore, provides immediate instruction as to how one would practically manufacture a plate corresponding to our model for testing. It may be helpful to the reader to consider our variation of porosity through a change in hole spacing as similar to the variation of acoustic impedance in traditional liners through a change of resonator depth (Jones *et al.* 2017). We note, however, this choice may lead to unphysical values of $\alpha_H > 1$ and in such a case, to design a corresponding practical experiment, variations of r and K_R would be necessary to achieve the same $\mu(x)$ values. We stress, it is only the overall porosity (impedance) variation of $\mu(x)$ that truly matters in this model, and, as a whole parameter, this always permits a physically relevant perforated surface. Our set-up is illustrated in figure 1.

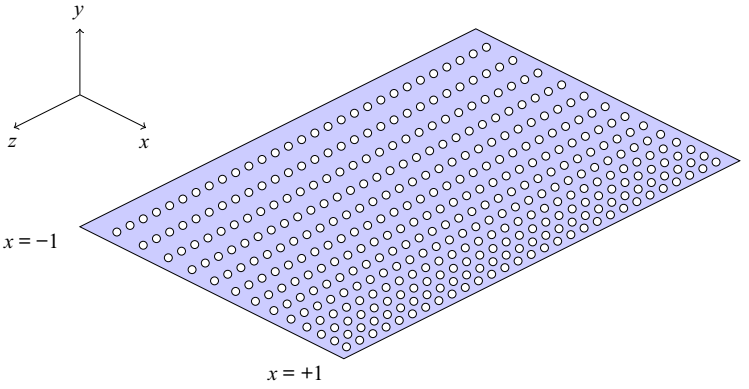

FIGURE 1. Schematic of the variable-porosity plate with edges at $x = -1$ and $x = 1$. The plate extends infinitely in the spanwise (z) direction.

2.1. *Mathieu function expansion*

Here, we now solve the problem using the Mathieu function collocation method of Colbrook & Priddin (2020) which provides an expansion of ϕ in Mathieu functions using separation of variables in elliptic coordinates. A full discussion of this method can be found in Colbrook & Priddin (2020), and user-friendly code for the method can be found at https://github.com/MColbrook/MathieuFunctionCollocation.

When using elliptic coordinates, $x = \cosh(\nu)\cos(\tau)$, $y = \sinh(\nu)\sin(\tau)$, the appropriate domain becomes $\nu \geq 0$ and $\tau \in [0, \pi]$. The Helmholtz equation with homogeneous Dirichlet boundary condition (the continuity condition) along $\{(x, y) : y = 0, |x| > 1\}$ and the Sommerfeld condition at infinity become

$$\left.\begin{aligned} \frac{\partial^2\phi}{\partial\tau^2} + \frac{\partial^2\phi}{\partial\nu^2} + \frac{\cosh(2\nu) - \cos(2\tau)}{2}k_0^2\phi = 0, \\ \phi|_{\tau=0} = \phi|_{\tau=\pi} \equiv 0, \\ \lim_{\nu\to\infty} \nu^{1/2}\left(\frac{\partial}{\partial\nu} - \mathrm{i}k_0\right)\phi(\nu, \tau) = 0. \end{aligned}\right\} \tag{2.3}$$

This set of equations does not currently impose the porosity (impedance) condition along the plate and so provides a general solution for any boundary condition on the plate. We shall discuss the application of our particular boundary condition shortly in § 2.2. To simplify the formulae, we let $\kappa = k_0^2/4$. Separation of variables for solutions of the form $V(\nu)W(\tau)$ leads to the regular Sturm–Liouville eigenvalue problem

$$\left.\begin{aligned} W''(\tau) + (\lambda - 2\kappa\cos(2\tau))\,W(\tau) = 0, \\ W(0) = W(\pi) = 0. \end{aligned}\right\} \tag{2.4}$$

The solutions of this are sine-elliptic functions, denoted by se_n with eigenvalue λ_n, which we expand in a sine series as

$$\mathrm{se}_n(\kappa; \tau) = \mathrm{se}_n(\tau) = \sum_{l=1}^{\infty} B_l^{(n)} \sin(l\tau). \tag{2.5}$$

This series converges absolutely and uniformly on all compact sets of the complex plane (Olver *et al.* 2010). The eigenfunctions are orthogonal, and we choose the normalisation

$$\int_0^{\pi} \mathrm{se}_m(\tau)\mathrm{se}_n(\tau)\,\mathrm{d}\tau = \frac{\pi}{2}\delta_{mn}. \tag{2.6}$$

We find the coefficients B_l^n via a simple Galerkin method. The corresponding $V(\nu)$ with the appropriate radiation condition at infinity are given by the Mathieu–Hankel functions

$$\mathrm{Hse}_n(\kappa;\,\nu) = \mathrm{Hse}_n(\nu) = \mathrm{Jse}_n(\nu) + \mathrm{iYse}_n(\nu).$$

These Mathieu–Hankel functions can be expanded in a series using Bessel functions (McLachlan 1964; Olver *et al.* 2010)

$$\mathrm{Hse}_n(\nu) = \sum_{l=1}^{\infty} \frac{(-1)^{l+n}B_l^{(n)}}{C_n}\left[J_{l-1}(\mathrm{e}^{-\nu}\sqrt{\kappa})H^{(1)}_{l+p_n}(\mathrm{e}^{\nu}\sqrt{\kappa}) - J_{l+p_n}(\mathrm{e}^{-\nu}\sqrt{\kappa})H^{(1)}_{l-1}(\mathrm{e}^{\nu}\sqrt{\kappa})\right], \tag{2.7}$$

where $p_n = (1+(-1)^n)/2$. Here, J_n denotes the Bessel function of the first kind of order n and $H_n^{(1)}$ denotes the Hankel function of the first kind of order n. The series in (2.7) converges absolutely and uniformly on all compact sets of the complex plane (Olver *et al.* 2010). We choose the normalisation constants C_n so that $\mathrm{Hse}_n'(0) = 1$.

The full general solution can then be written as

$$\phi(\nu,\tau) = \sum_{n=1}^{\infty} a_n \mathrm{se}_n(\tau)\mathrm{Hse}_n(\nu), \tag{2.8}$$

where a_n are unknown coefficients. These coefficients are determined by applying the appropriate boundary condition along the plate, which we do so in § 2.2.

Given the Bessel function expansion of $\mathrm{Hse}_n(\nu)$ in (2.7), we can directly compute the far-field directivity $D(\theta)$ from (2.8) using asymptotics of Bessel functions. In the appropriate limit, τ becomes the polar angle θ, whereas ν becomes $\cosh^{-1}(r)$ (where (r,θ) denote the usual polar coordinates). This leads to

$$D(\theta) = \sqrt{\frac{2}{\pi k_0}}\sum_{n=1}^{\infty}\frac{a_n B_1^{(n)}}{C_n}\exp\left(\frac{(2p_n-3)\pi}{4}\mathrm{i}\right)\mathrm{se}_n(\theta). \tag{2.9}$$

An advantage of our approach is that we implicitly compute a sine series for the far-field directivity $D(\theta)$ through the sine-elliptic functions $\mathrm{se}_n(\theta)$ given by (2.5).

Finally, we define the total far-field noise, measured in dB, as

$$P = 10\log_{10}\left(\int_0^{\pi}|D(\theta)|^2\,\mathrm{d}\theta\right), \tag{2.10}$$

which may be computed numerically from the series expansion for $D(\theta)$.

2.2. *Employing the boundary conditions*

Here, we now determine the unknown coefficients a_n in the expansion (2.8), as required for our particular boundary condition (2.2). We do so by adopting a spectral collocation

method to calculate their approximate value. Throughout, we denote the approximate coefficients by $\tilde{a}_n$.

We take our general solution (2.8) and substitute into (2.2), written in original (x, y) coordinates. We truncate the expansion at N terms to obtain the approximate condition

$$\sum_{n=1}^{N} \tilde{a}_n \mathrm{se}_n\left(\cos^{-1}(x)\right)\left[1 - 2\,\mathrm{Hse}_n(0)\mu(x)\sqrt{1-x^2}\right] = -\sqrt{1-x^2}\cdot\frac{\partial \phi_I}{\partial y}(x). \tag{2.11}$$

We now evaluate this at chosen collocation points,

$$x = \cos\left(\frac{2j-1}{2N}\pi\right), \quad j = 1, \ldots, N, \tag{2.12}$$

which correspond to Chebyshev points in Cartesian coordinates and equally spaced points in elliptic coordinates (Trefethen 2000; Boyd 2001). This gives rise to an $N \times N$ linear system for the unknown coefficients $\{\tilde{a}_n\}_{n=1}^{N}$, which we precondition by rescaling to ensure that each row of the resulting matrix has a constant l^1 vector norm.

2.3. *Avoiding numerical cancellations*

The terms in the series (2.7) can easily be evaluated for small l. However, for large l, the terms in the series suffer from underflow and overflow associated with cancellations between the Bessel and Hankel functions. For large l and fixed $x \in \mathbb{R}_{>0}$ we use the asymptotics

$$\left.\begin{aligned} J_l(x) &= \sum_{j=0}^{m} \frac{(-1)^j}{j!(j+l)!}\left(\frac{x}{2}\right)^{2j+l} + O\left(\frac{1}{(m+l+1)!}\right), \\ H_l^{(1)}(x) &= \frac{-\mathrm{i}}{\pi}\left(\frac{2}{x}\right)^{l}\sum_{j=0}^{m}\frac{(l-j-1)!}{j!}\left(\frac{x}{2}\right)^{2j} + O\left((l-(m+2))!\right), \end{aligned}\right\} \tag{2.13}$$

valid as $l \to \infty$. For fixed $a, b \in \mathbb{Z}$, this gives the asymptotic form

$$\begin{aligned} &J_{l+a}(\mathrm{e}^{-\nu}\sqrt{\kappa})H_{l+b}^{(1)}(\mathrm{e}^{\nu}\sqrt{\kappa}) \\ &\quad= \frac{-\mathrm{i}}{\pi}\left(\frac{\sqrt{\kappa}}{2}\right)^{a-b}\exp(-\nu(2l+a+b))\left[\sum_{j=0}^{m}\frac{(-1)^j(l+a)!}{j!(j+l+a)!}\left(\frac{\mathrm{e}^{-\nu}\sqrt{\kappa}}{2}\right)^{2j}\right] \\ &\qquad\times\left[\sum_{j=0}^{m}\frac{(l+b-j-1)!}{j!(l+a)!}\left(\frac{\mathrm{e}^{\nu}\sqrt{\kappa}}{2}\right)^{2j}\right] + O\left(l^{-(m+2)}\right). \end{aligned} \tag{2.14}$$

We found this to be an excellent approximation for large l. It can also be accurately evaluated for moderate m since the terms $(l+a)!/(j+l+a)!$ and $(l+b-j-1)!/(l+a)!$ can be evaluated as products of j and $|j+1+a-b|$ terms respectively. In what follows, we typically used this asymptotic form when $l > 100$ and took up to $m = 5$ terms. When plotting errors of our method, we were careful to compare against converged computations for which the series (2.7) was evaluated directly using extended precision (such checks were the only place where we made use of extended precision).

3. Theoretical calculation of lift

Here, we briefly review the theory of Hajian & Jaworski (2017) to calculate the lift coefficient of a porous plate, where the porosity is permitted to vary along the chord. Note, this does not account for the full aerodynamics since we are not calculating drag.

We suppose a flat-plate aerofoil is placed in uniform upstream flow of speed $U_{inf}\boldsymbol{e}_x$, where $\boldsymbol{e}_x$ denotes the horizontal direction. We let $z_a(x)$ denote the camber line of the plate, which for our case of a flat plate at fixed angle of attack α ensures $\mathrm{d}z_a/\mathrm{d}x = -\alpha$. Under the assumption of small disturbance (neglecting $O(\alpha^2)$), the plate lies in the region $-1 \leq x \leq 1$ where, once again, lengths are non-dimensionalised by semi-chord.

Assuming a Darcy-type boundary condition, we may connect the pressure jump to the local normal flow rate through the plate, w_s:

$$w_s = -C\mathcal{R}(x)(p_u - p_l), \tag{3.1}$$

where C is defined as a porosity coefficient, and $\mathcal{R}(x) = \alpha_H(x)$ is the porosity distribution (Hajian & Jaworski 2017, (2.9)). The integral equation linking the pressure jump to the camber line and porosity distribution in thence given by

$$\rho_f U_{inf} C\mathcal{R}(x)p(x) - \frac{1}{2}\fint_{-1}^{1} \frac{p(t)}{t-x}\,\mathrm{d}t = 2\frac{\mathrm{d}z_a}{\mathrm{d}x}, \tag{3.2}$$

where pressure is non-dimensionalised by $(\rho_f U_{inf}^2)/2$. (Note this is different to the non-dimensionalisation for the acoustics where pressure is non-dimensionalised with respect to speed of sound). This equation is solved to yield

$$\begin{aligned} p(x) = {} & \frac{4\psi(x)}{1+\psi^2(x)}\frac{\mathrm{d}z_a}{\mathrm{d}x} - \frac{4}{\pi\sqrt{1+\psi^2(x)}}\exp\left(\fint_{-1}^{1}\frac{k(\psi(t))}{t-x}\,\mathrm{d}t\right) \\ & \times \int_{-1}^{1} \frac{\mathrm{d}z_a/\mathrm{d}t}{\sqrt{1+\psi^2(t)}\exp\left(\fint_{-1}^{1}\dfrac{k(\psi(\xi))}{\xi-t}\,\mathrm{d}\xi\right)(x-t)}\,\mathrm{d}t, \end{aligned} \tag{3.3}$$

where $\psi(x) = 2\rho_f U_{inf} C\mathcal{R}(x)$, and $k(y) = \pi^{-1}\cot^{-1}(y)$. Implementation and validation by comparison with Hajian & Jaworski (2017) is discussed shortly.

4. Flow resistivity through wings

To provide an initial porosity distribution along a flat plate, we consider the distributions that appear in nature, in particular for barn owns and common buzzards.

4.1. *Experimental measurements*

In order to obtain quantitative data on the permeability of owl wings compared to the wings of other, non-silently flying birds of prey, measurements of the flow resistance were conducted on a set of prepared wing specimen. For measurements on porous materials according to ISO 9053 (1991), the materials have to be cut into cylindrical samples of constant thickness and tightly fitted into a sample holder. Since that is obviously not possible for prepared bird wings, which may consist of only a single layer of feathers especially close to the trailing edge (see, for example, the work of Nachtigall & Klimbingat (1985) and Bachmann, Mühlenbruch & Wagner (2011)), a special measurement head

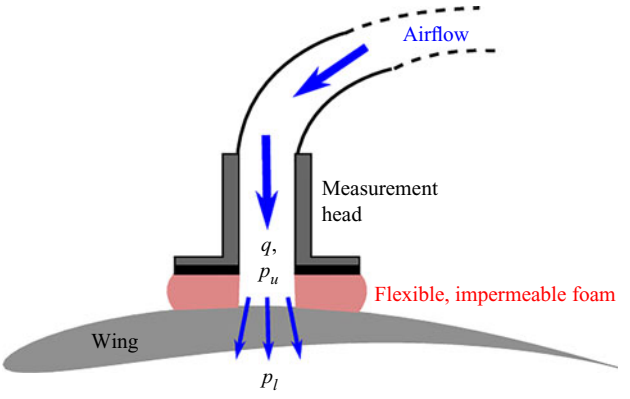

FIGURE 2. Set-up used to measure the wing air flow resistance R (4.1).

was constructed. It can be pressed onto the surface of the wings with a defined force, allowing one to seal off the area of contact between the planar measuring head and the feather surface. With the help of this measurement head, a defined air flow with a volumetric airflow rate q (in $\mathrm{m}^3\,\mathrm{s}^{-1}$) is conducted through the prepared wing (see figure 2). The air flow resistance R at this position of the wing is then calculated from the resulting static pressure difference across the wing

$$R = \frac{p_u - p_l}{q}. \tag{4.1}$$

Such measurements were conducted at each chosen wing location for seven different volume flows. According to ISO 9053 (1991), the resulting value of the air flow resistance was then obtained by linear extrapolation of the results to a low flow speed of $5 \times 10^{-4}\ \mathrm{ms}^{-1}$.

4.2. *Theoretical modelling*

We must relate the experimentally recovered values of flow resistance, R, to both the aeroacoustic porosity parameter μ, and the aerodynamic parameter, C. We begin with the aeroacoustic parameter μ. Recall that $\mu(x) = \alpha_H(x)K_R/(\pi r^2)$, where we assume the porosity is created by circular apertures of constant radius, r, and, for a plate with circular apertures, the Rayleigh conductivity of the plate, $K_R = 2r$. However, for an arbitrary material, K_R is defined as $K_R = Q/(\phi_u - \phi_l)$, where $Q = \mathrm{d}q/\mathrm{d}t$ is the volume flux through the plate. Hence for the wing in harmonic flow, $K_R = \omega^2\rho_f/R$. We thus have two ways of calculating $\mu(x)$

$$\mu(x) = \alpha_H(x)\frac{2}{\pi r}, \quad \mu_{exp}(x) = \alpha_H^{exp}\omega^2\rho_f\frac{1}{R}\frac{1}{\pi r_{exp}^2}, \tag{4.2a,b}$$

where α_H denotes the open area ratio of circular apertures or radius r in a flat plate, α_H^{exp} denotes the open area ratio of pores of typical radius r_{exp} in a wing, and R is the measured flow air flow resistance. We may thus equate the two to provide values for $\alpha_H(x)$ to input

into our model

$$\alpha_H(x) = \frac{\omega^2 \rho_f r \alpha_H^{exp}}{2R r_{exp}^2}. \tag{4.3}$$

We shall assume that the chordwise variation in (4.3) arises only due to the air flow resistance, R, and that α_H^{exp} and r_{exp} are constant. According to Jaworski & Peake (2013) we take the value $\alpha_H^{exp} = 0.0014$. This value arises from the trailing-edge brush experiment of Herr (2007) wherein polypropylene fibres with physical properties similar to the feather keratin of owl wings are used to investigate noise reduction. The fibres which exhibited the best noise reduction were converted to the equivalent open area ratio parameter of $\alpha_H^{exp} = 0.0014$ by Jaworski & Peake (2013). Since in Jaworski & Peake (2013) lengths are non-dimensionalised by a bending wave number (which does not feature in our analysis since our plate is not flexible), it is more difficult to determine the corresponding value of r_{exp}. We, therefore, turn to detailed measurements made on the wings of barn owls by Bachmann, Wagner & Tropea (2012), which results in a value of $r_{exp} = 5.5 \times 10^{-4}$ m. This arises from supposing for a given barn owl feather there are two fringes per mm (Bachmann *et al.* 2012) (and thus two gaps between the fringes per mm) and the total length of the vane of the feather is between 12.5 and 15 cm (Bachmann, Klän & Baumgartner 2007). Therefore each feather has between 250 and 300 apertures in the chordwise direction. We select r_{exp} as the mid-value, supposing each aperture is $1/275$ of our fixed 15 cm chord.

For the theoretical model, we shall suppose a manufactured flat plate has holes with radius $r = 1$ mm, which is practical to construct, and we use a typical frequency of $\omega =$ 500 Hz to complete our relationship between R and $\alpha_H(x)$ since we wish to focus on low-frequency noise reductions. Assuming the area of measurement over the wing was 1 cm^2, we obtain a value of $C = 0.016$ for the porosity coefficient required in the lift calculations. We shall use the same value of the parameter group $\alpha_H^{exp}/(\pi r_{exp}^2)$ (which can be viewed as the closed area of the wing) for the owl and buzzard as input to obtain our model, $\alpha_H(x)$. Whilst this is unlikely to be true for the buzzard, it provides an upper bound on the value of α_H to input to our model, as it is clear from detailed wing pictures (Chen *et al.* 2012) that the closed area of the buzzard's wing is greater than that for the owl.

5. Results

5.1. *Bio-inspired distributions*

In this section, the results from the air flow resistance measurements on the prepared wings are summarised and converted to their corresponding α_H values. Overall, five wings of the barn owl (*tyto alba*) and nine wings of the common buzzard (*buteo buteo*) were investigated to obtain the data used in the present study. For each wing, measurements were made at up to eight different positions, from which the first four were located in the region of the primary and secondary remiges, and hence closer to the trailing edge, while the last four were located closer to the leading edge, on the primary and secondary coverts. Figure 3 illustrates the locations at which samples were taken for Wing 3 of the barn owl. Table 1 summarises the results for the barn owl wings and table 2 those of the buzzard wings.

We plot the variation in α_H along the chord of each wing in figure 4, as calculated from experimental measurements and using (4.3). For microphones close to the wing tips (typically microphone position P1 as seen in figure 3), where the chord length is substantially different to the main wing, we have neglected those results, since our two-dimensional model cannot capture any spanwise variation in either wing shape

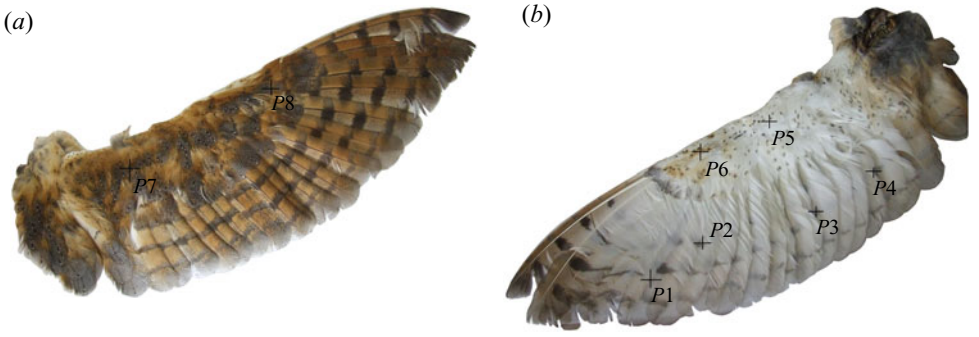

FIGURE 3. Upper and lower side of Wing 3 of the barn owl samples, showing the positions at which air flow resistance was measured.

	Air flow resistance (kPa s m^{-3})							
Position	1	2	3	4	5	6	7	8
Wing 1	1978	—	1749	1413	13 650	15 388	11 460	7505
Wing 2	2812	3647	2685	1819	14 085	9148	13 343	7043
Wing 3	1742	3244	1992	1456	11 286	14 707	10 064	9620
Wing 4	1824	3356	1774	2476	9167	6063	15 027	7064
Wing 5	1067	1726	1592	1728	3515	6513	8636	4329

TABLE 1. Air flow resistance of the barn owl wings.

	Air flow resistance (kPa s m^{-3})							
Position	1	2	3	4	5	6	7	8
Wing 1	3910	3916	3864	4117	10 106	10 564	10 329	9026
Wing 2	4130	4242	3219	3934	—	11 964	9054	7545
Wing 3	3499	3743	4093	4389	9106	11 359	6997	9111
Wing 4	4994	3773	3948	4767	8161	12 106	7748	9721
Wing 5	3367	3304	3235	3164	12 005	8504	19 200	9249
Wing 6	4347	3705	2963	3872	9216	12 495	10 455	10 389
Wing 7	3141	3675	3516	3815	13 177	12 445	10 111	11 100
Wing 8	3374	3533	3612	3232	14 539	8692	10 180	13 297
Wing 9	3502	3440	4057	5008	13 910	15 121	17 296	9987

TABLE 2. Air flow resistance of the buzzard wings.

or morphology. The chord length is measured from the photographic microphone locations using Matlab's image viewer app, as illustrated in figure 5. There is an outlier in the porosity data from the owl at a chord of $\sim$60 %. This outlier is due to the fact that these wings are biological systems and as such, not perfectly homogeneous. As mentioned before, this is especially true close to the trailing edge, where the wings consist only of one or two layers of feathers.

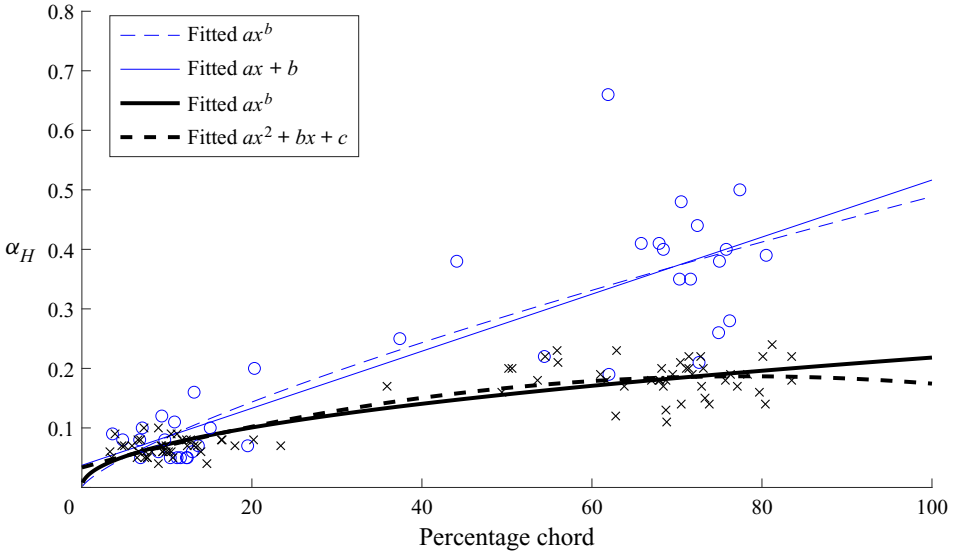

FIGURE 4. Porosity, α_H, as calculated from (4.3) from the measurement data for owls (blue, circles) and buzzards (black, crosses). Best fit curves are given according to Matlab's fit command.

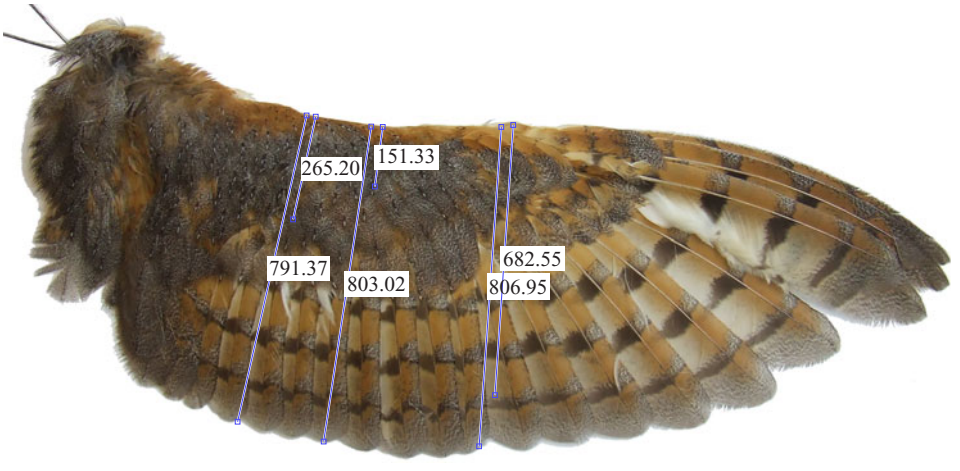

FIGURE 5. Chord locations are measured from photographs using Matlab's image viewer app. Lengths are given in terms of the number of pixels.

Lines of best fit are produced using Matlab's fit command; both polynomial and exponential fitting were considered, and the best-fitting lines from each reproduced in figure 4. From these we shall take the variation which appears most likely in the owl wing to be

$$\alpha_H^{owl} = 0.037 + 0.48\left(\frac{x}{2} + \frac{1}{2}\right), \tag{5.1}$$

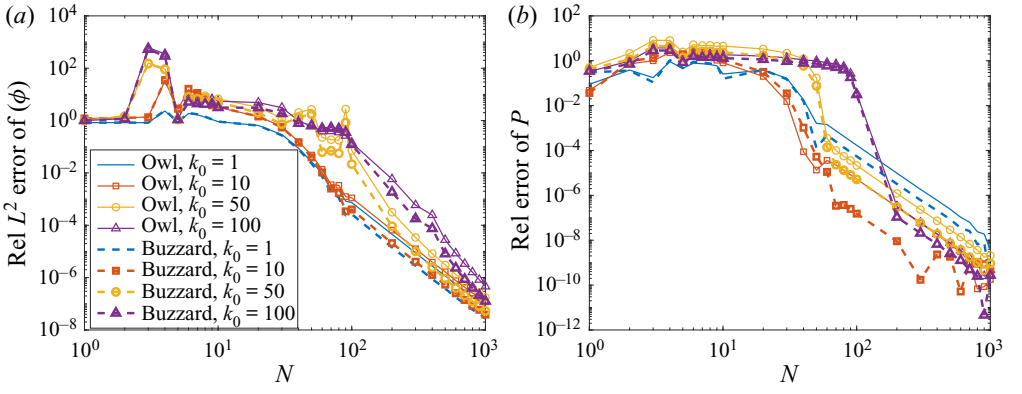

FIGURE 6. Relative errors for $[\phi]$ (a, L^2 norm error over $[-1, 1]$) and SPL (b). The method has a high order of algebraic convergence, allowing us to compute physical values to several significant figures.

and for the buzzard

$$\alpha_H^{buzz} = 0.22\left(\frac{x}{2} + \frac{1}{2}\right)^{0.48}, \tag{5.2}$$

recalling that our chord lies in the region $x \in [-1, 1]$.

5.2. *Numerical convergence and validation of methods*

5.2.1. *Acoustic calculations*

To demonstrate convergence for the acoustic solution, in figure 6 we have plotted the relative errors against N (the number of basis functions used) for the values of α_H^{owl} and α_H^{buzz}. These errors were estimated by comparing with values computed for larger N. We have plotted the relative error in the L^2 norm of $[\phi]$ (the jump in the field across the plate) and the P values for a quadrupole source. This shows convergence for a wide range of frequencies and also shows that we can easily gain several digits of relative accuracy.

To validate the acoustic calculations, we recreate figure 7(b) from Cavalieri *et al.* (2016) for a uniformly porous plate in figure 7, which shows excellent agreement. Note, our non-dimensionalisation of length is by semi-chord, whereas Cavalieri *et al.* (2016) use chord, therefore the values of k_0 and α_H/R which we use are half the values from Cavalieri *et al.* (2016). For this figure, we place a quadrupole at $(1, 0.008)$, corresponding to the non-dimensional location of $(1, 0.004)$ used by Cavalieri *et al.* (2016).

5.2.2. *Aerodynamic calculations*

We recall that the pressure jump is given by (3.3), and the (non-dimensionalised) lift is then given by the integral

$$L = -\int_{-1}^{1} p(x)\,\mathrm{d}x, \tag{5.3}$$

where the minus sign corresponds to the pressure jump being taken to be $p_u - p_l$. To calculate this, we need an accurate and efficient method to compute iterates of the Hilbert transform. We used two approaches, which enables us to estimate the accuracy of our

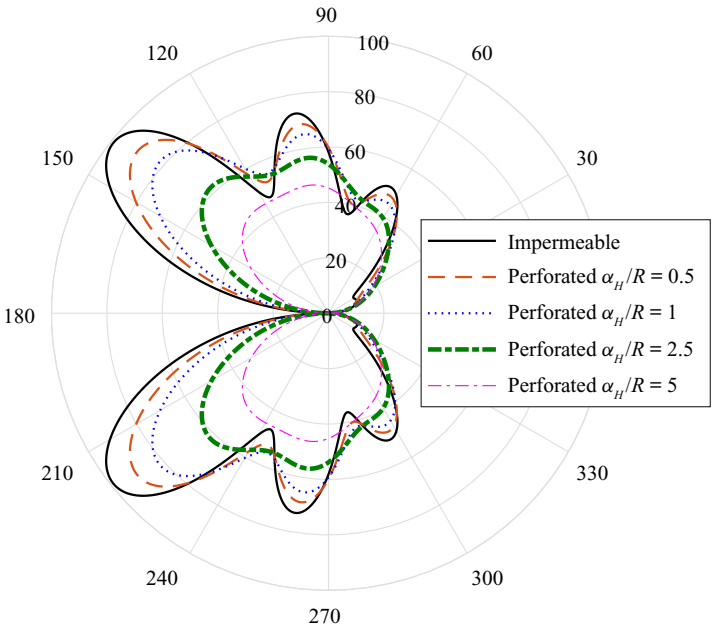

FIGURE 7. Directivity, $|D(\theta)|$, for $k_0 = 5$ for uniformly porous plates. This shows excellent agreement with figure 7(*b*) from Cavalieri *et al.* (2016).

estimate through comparison. To ease the exposition, we only discuss the computation of the integral

$$g(x) = \fint_{-1}^{1} \frac{f(t)}{t - x}\,\mathrm{d}t, \tag{5.4}$$

for $x \in (-1, 1)$ and sufficiently regular f (e.g. integrable and locally Hölder continuous in $(0, 1)$).

For the first method, we use a standard subtraction technique and consider the function

$$h(x, t) := \frac{f(t) - f(x)}{t - x}. \tag{5.5}$$

We use the fact that, for sufficiently regular f and for $x \in (-1, 1)$, $h(x, t)$ is integrable over $t \in [-1, 1]$ with

$$g(x) = \int_{-1}^{1} h(x, t)\,\mathrm{d}t + f(x) \log\left(\frac{1 - x}{1 + x}\right). \tag{5.6}$$

We compute the integral of h using global adaptive quadrature through MATLAB's integral command, keeping track of the tolerances when iterating the procedure.

Our second approach is to make use of spectral methods based on Chebyshev polynomials, conveniently handled via the Chebfun software package (Driscoll, Hale & Trefethen 2014). We first expand the function $f(t)\sqrt{1 - t^2}$ in Chebyshev polynomials of the first kind, $T_n(\cdot)$. These have the useful property that

$$\fint_{-1}^{1} \frac{T_n(t)}{(t - x)\sqrt{1 - t^2}}\,\mathrm{d}t = \pi U_{n-1}(x), \tag{5.7}$$

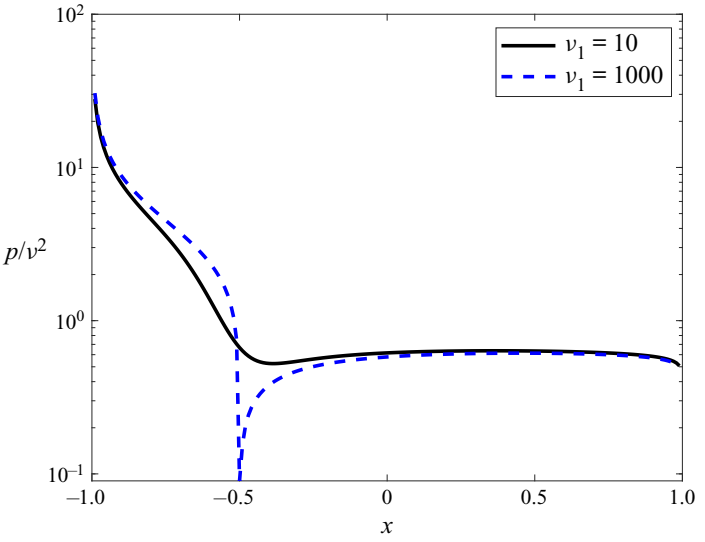

FIGURE 8. Pressure distribution for $\nu_1 = 10$ and $\nu_1 = 1000$, showing excellent agreement with the results of Hajian & Jaworski (2017).

where $U_n(\cdot)$ denote Chebyshev polynomials of the second kind (see (18.17.42) of Olver *et al.* 2010). We can thus compute an expansion of g in Chebyshev polynomials of the second kind. We can iterate this procedure, taking advantage of rapid algorithms for computing the Chebyshev coefficients of $g(x)\sqrt{1-x^2}$ given the expansion of g.

To verify our approach, we reproduce the results of Hajian & Jaworski (2017), where

$$\psi(x) = \frac{5}{2}\left(1 + \tanh\left(\nu_1\left(x + \frac{1}{2}\right)\right)\right), \quad \frac{\mathrm{d}z_a}{\mathrm{d}x} = \nu_2, \tag{5.8a,b}$$

for constants ν_1, ν_2. Figure 8 shows the results for $\nu_1 = 10$ and $\nu_1 = 1000$, with excellent agreement with figure 2 of Hajian & Jaworski (2017).

5.3. *Bio-inspired results*

Having validated our numerical methodology and shown results in agreement with previous work, we now present the acoustic results for the bio-inspired spanwise variations. In figure 9 we show the difference in far-field noise, $\Delta P = P^{owl} - P^{buzz}$ for P defined by (2.10), generated for a near-field quadrupole source located at (x_0, y_0) which models a turbulent trailing-edge source. The incident potential is therefore given by

$$\phi_I = \frac{\mathrm{i}k_0^2}{4r_0^2}(x - x_0)(y - y_0)H_2^{(1)}(k_0 r_0), \tag{5.9}$$

where $r_0 = \sqrt{(x-x_0)^2 + (y-y_0)^2}$, and $H_n^{(1)}$ are Hankel functions of the first kind.

It is perhaps no surprise to see that, via this model, the owl is predicted to produce less trailing-edge noise than the buzzard given that the trailing edge of the owl's wing is far more porous (has a higher α_H value) than that of the buzzard's. This is particularly true for low frequencies which are known to be significantly reduced by porosity (Jaworski & Peake 2013), however, the total level of low-frequency noise reduction is intrinsically

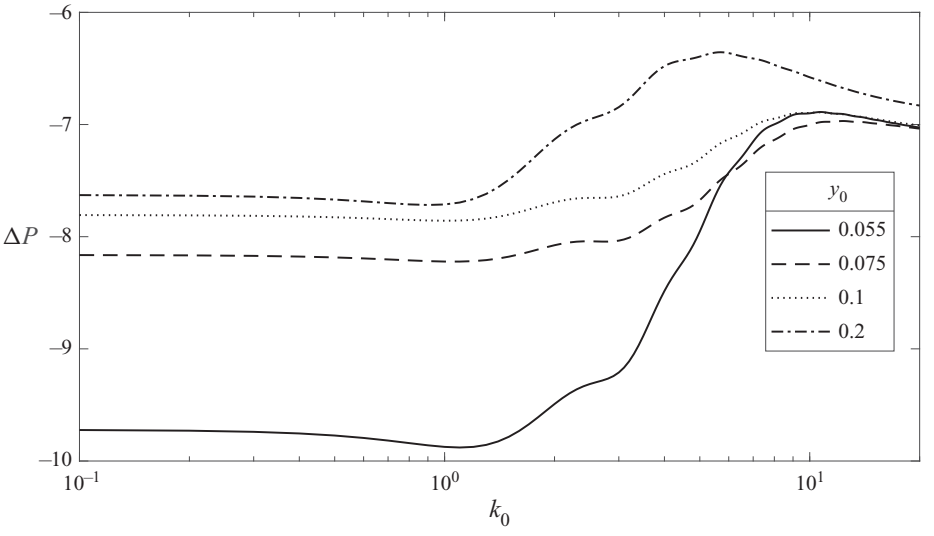

FIGURE 9. Value of ΔP for a near-field quadrupole source at $x_0 = 0.95$ and various y_0. Negative values indicate the owl is quieter than the buzzard by that many dB.

linked to the vertical location of the quadrupole source. At higher frequencies, the owl is predicted to produce only 7 dB less trailing-edge noise, and this is similar across all quadrupole locations. We cannot currently extend this analysis to frequencies much higher than $k_0 = O(10)$ since outside of this range the asymptotic requirements for the homogenised boundary condition may not hold (Howe 1998).

We first compare our theoretical model to the noise reduction achieved by uniformly porous aerofoils in Geyer & Sarradj (2014, figure 8, lowest panel); there a low-frequency noise reduction of up to ∼10 dB is reported for a porous aerofoil with low resistivity (high porosity) versus a porous aerofoil with high resistivity (low porosity). As frequency increases, the noise reduction diminishes, and in some cases, a noise increase is observed (largely due to surface roughness). This is in broad agreement with our theoretical results comparing the owl (low resistivity at the trailing edge) to the buzzard (comparatively higher resistivity at the trailing edge), although it does not account for any features of continuously varying porosity.

Next, we compare our predicted noise reduction to that measured experimentally for owl and buzzard wings in Geyer, Sarradj & Fritzsche (2013), and Sarradj, Fritzsche & Geyer (2010). The measurements from Geyer *et al.* (2013) were performed in an anechoic wind tunnel using microphone array techniques and acoustic beamforming (the same set-up as used in Geyer & Sarradj (2014) for the uniformly porous aerofoils). As an example, figure 10 shows a schematic of the experimental set-up used by Geyer *et al.* (2013) as well as the sound pressure level difference between the results obtained for a buzzard wing and a barn owl wing of similar size (wings numbers 2 and 10 from Geyer *et al.* 2013). For low to moderate frequencies, the measured noise reduction is between 4 and 12 dB, whilst for higher frequencies, the noise reduction can exceed 20 dB. In the flyover measurements on living birds (Sarradj *et al.* 2010), however, smaller noise reductions between 3 dB at medium frequencies (around 1.6 kHz, $k_0 \approx 2$) to 8 dB at higher frequencies (6.3 kHz, $k_0 \approx 8.5$) have been obtained for the gliding flight noise from a barn owl compared to that from a Harris's hawk and a common kestrel (Sarradj *et al.* 2010).

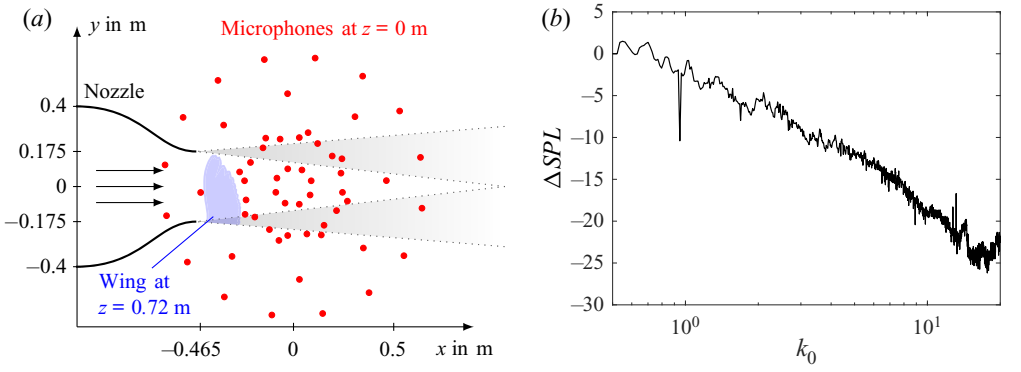

FIGURE 10. Schematic of the experimental set-up (*a*) and resulting ΔSPL between a buzzard wing and a barn owl wing at a flow speed of approximately 13 ms^{-1} (*b*) Geyer *et al.* (2013). Negative values indicate the owl is quieter than the buzzard by that many dB.

These results differ greatly from the porous aerofoil results in Geyer & Sarradj (2014), particularly at high frequencies since there are numerous other silent-flight designs on the owl's wing which are not modelled by porosity alone, such as leading-edge combs, serrations and canopies, all of which may alter the owl's noise reduction at different frequencies (Jaworski & Peake 2020). At high frequencies, serrations are particularly effective for noise reduction, with Moreau & Doolan (2013) observing up to 13 dB of noise reduction. Thus we anticipate the divergence of the theoretical predictions and the experimental results to be at least in part due to the serrated feature of the owl's wing. In addition, acoustic absorption by the owl's downy coat may play a role at high frequencies.

For comparison to owl wing noise, we therefore only concern ourselves with the low-to-moderate-frequency behaviour. Our theory overpredicts the noise reduction versus the realistic wing experimental measurements by up to 7 dB. This discrepancy at low frequencies may be due to the distortion of the flow over the wings (the three-dimensional behaviour) which has a significant effect on owl-generated noise since their leading-edge comb deflects the surface flow towards the wing tips. Geometric features such as the specific camber and thickness of the wing may also play a role. These features, which are lacking in our model, are also not taken account of in the porous aerofoil noise measurements in Geyer & Sarradj (2014), which similarly disagree with the realistic wing measurements. We, therefore, believe our results correctly predict the effects of porosity along on aerofoil noise, but cannot represent the true total noise reduction of realistic wings due to a number of additional noise-reduction features present on realistic owl wings.

In figure 11 we consider the effects of the owl versus buzzard distributions on leading-edge noise, and see surprisingly that the owl distribution also would produce less leading-edge noise despite the two wings having similar leading-edge porosity values. We consider an incident gust by selecting a potential satisfying $\partial\phi_I/\partial y|_{y=0} = -\mathrm{e}^{\mathrm{i}\delta x}$, where $\delta = k_1/\sqrt{1-M^2}$, and $k_1 = \sqrt{1-M^2}k_0/M$ thus the Helmholtz number, k_0, is δM, such that the gust convects from upstream with the mean flow with Mach number M. Full details of why this is the case may be found readily in the literature for leading-edge noise (Tsai 1992; Ayton & Kim 2018). We assume the same impedance style boundary condition, (2.2), noting that here the low Mach number approximation has been used. The difference in leading-edge noise levels is given in figure 11, for $M = 0.05$. We notice that, again, the owl is quieter than the buzzard for low frequencies, however, now the reduction is only

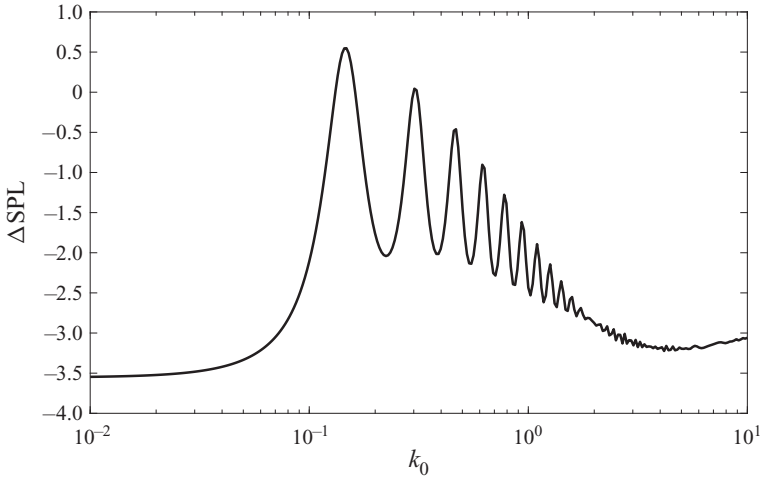

FIGURE 11. Value of ΔP for an incident gust. Negative values indicate the owl is quieter than the buzzard by that many dB.

approximately 3.5 dB. Note the frequency range difference between the trailing-edge noise and the leading-edge noise; trailing-edge noise is a high-frequency phenomenon, whilst leading-edge noise is more dominant at lower frequencies. The lowest-frequency flyover noise reductions (Sarradj *et al.* 2010) of 3 dB are in agreement with our leading-edge noise-reduction predictions. However, it is unclear how much noise produced during the flyover tests can be attributed to each edge.

We now turn to the steady pressure distribution along the flat plates with prescribed porosity (5.1) and (5.2), which can be seen in figure 12. At an angle of attack $5.7^\circ = 0.1$ rad, the corresponding lift coefficients are 1.131 for the buzzard type, and 1.031 for the owl type, which are obtained by integrating the surface pressure given by (3.3). This is, of course, not the whole story for the actual owl and the buzzard, as they will have wings of different camber which significantly influences lift. Geyer *et al.* (2013) have measured the mean lift coefficient of barn owls, $\bar{C}_L = 0.185$, and buzzards, $\bar{C}_L = 0.084$ at zero angle of attack and a flow speed of approximately 13 ms^{-1}, indicating the camber of the wing greatly enhances the lift for the owl. The effect of camber of the owl's wing, therefore, may mitigate the aerodynamic penalty from the more porous trailing edge. It is, however, beyond the scope of the current paper to include camber in our models.

5.4. *Monotonic distributions*

Here we investigate the effect of the precise distribution of porosity in the interior of the plate on trailing-edge noise. We consider varying porosity along a flat plate through the model

$$\alpha_H(x) = \alpha_L + (\alpha_T - \alpha_L)\left(\frac{x}{2} + \frac{1}{2}\right)^{\gamma}, \tag{5.10}$$

where $\alpha_{L,T}$ denote the open area ratios at the leading and trailing edge, respectively. We consider only the case $\alpha_T \geq \alpha_L$, whereby the trailing edge has the same or greater porosity than the leading edge, as is observed from our wing measurements. We vary γ from $\gamma = 0.1$, where the porosity very rapidly changes at the leading edge, to $\gamma = 4$, where the porosity changes slowly at the leading edge. Sample variations are illustrated in figure 13

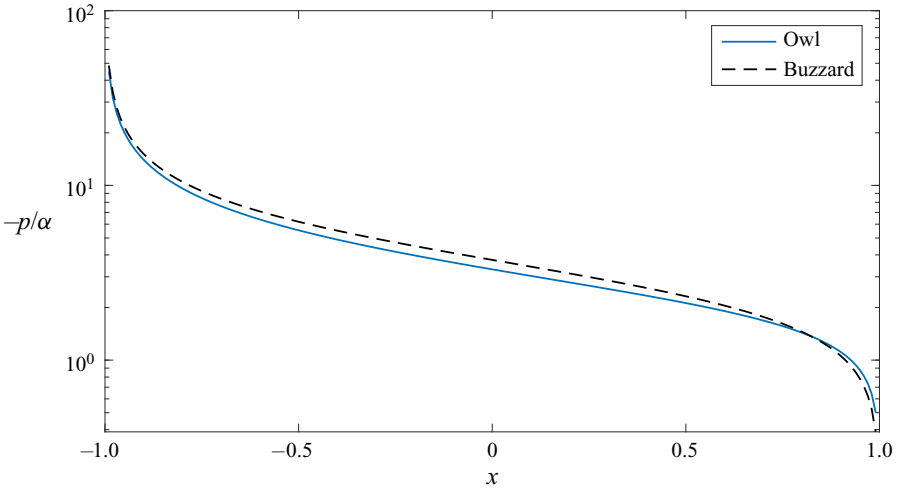

FIGURE 12. Steady pressure along the plate, divided by angle of attack, for the owl and buzzard porosity distributions.

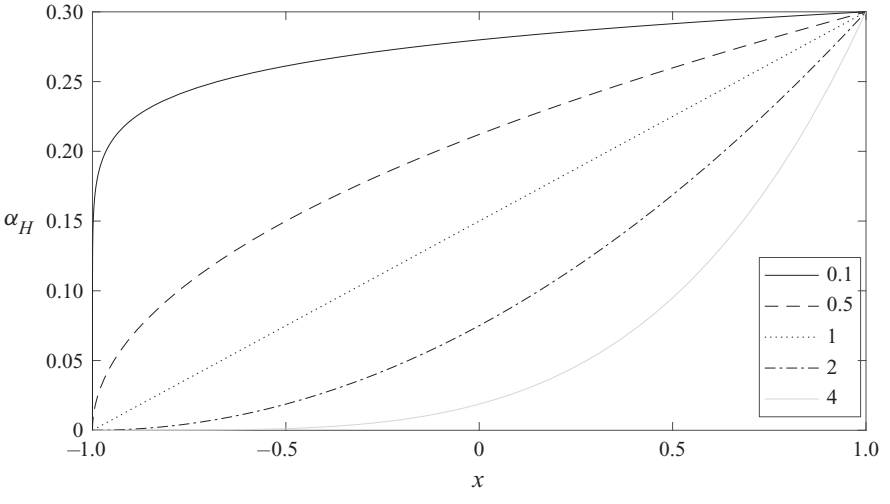

FIGURE 13. Monotonic porosity distributions $\alpha_H(x) = 0.3(x/2 + 1/2)^\gamma$ for various values of γ, corresponding to $\alpha_L = 0$ and $\alpha_T = 0.3$.

for $\alpha_L = 0$ and $\alpha_T = 0.3$. Note that this choice of variation means the average porosity for the whole wing is greater for a lower value of γ than a higher value of γ.

We focus on trailing-edge noise, using the same quadrupole source as (5.9) with $x_0 = 0.95$ and $y_0 = 0.05$ unless otherwise specified, and $M = 0.05$. We plot the varying lift and sound in figure 14 for $\alpha_L = 0$ and $\alpha_T = 0.3$; the acoustics show the effects at different frequencies. The acoustic results have been normalised by P_{TE}, corresponding to the value P would take if the whole plate had a constant porosity of α_T, i.e. when $\gamma = 0$. Thus a positive value indicates allowing for a monotonic reduction of porosity along the chord from the trailing-edge results in additional noise than if the porosity remained consistently at the trailing-edge value for the entire chord. The level of radiated noise is influenced by

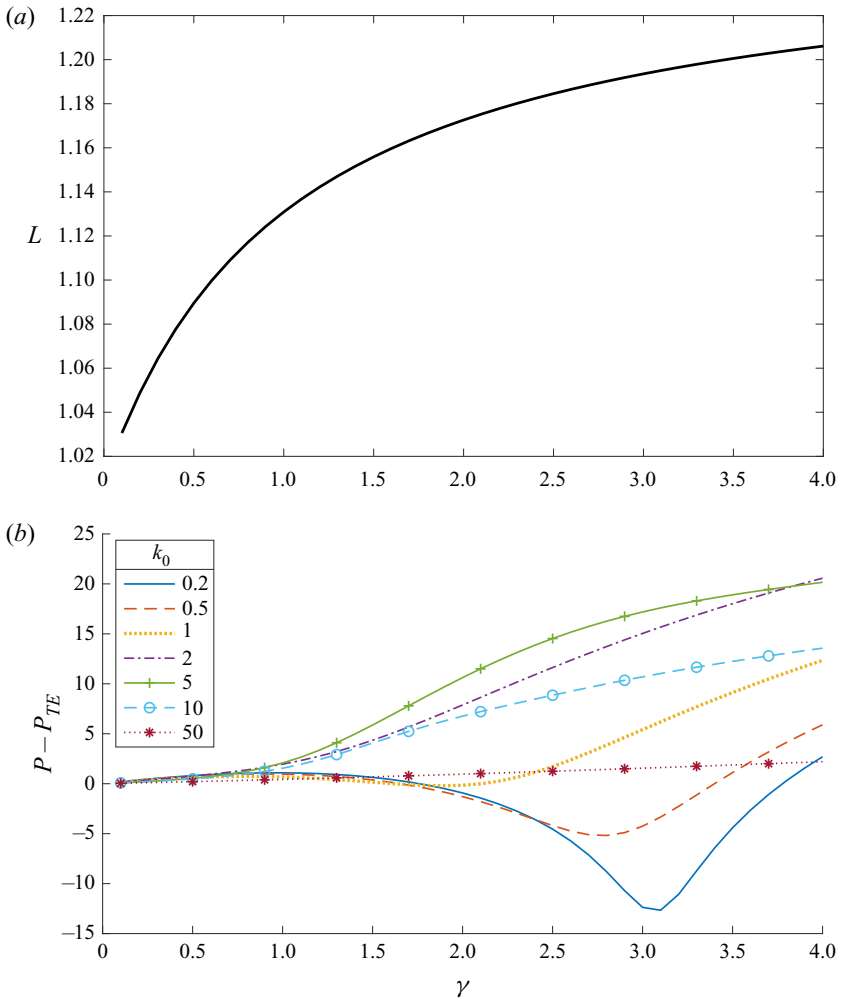

FIGURE 14. Effect of different monotonic variations of porosity from $\alpha_H = 0$ to 0.3 on lift coefficient at 0.1 rad angle of attack (*a*) and on trailing-edge noise (*b*).

both frequency and distribution of porosity, whilst the lift coefficient, $L = -\int_{-1}^{1} p(x)\,\mathrm{d}x$, increases monotonically with increasing γ: the lower the average porosity of the wing, the greater the lift, as would be anticipated.

Given the seemingly complicated frequency dependence of the scattered noise, we now consider two further cases in figures 15 and 16. In figure 15 we vary α_H from 0 to 0.1 and see a similar variation in noise as the previous case of figure 14; the lowest frequencies (0.2,0.5) have values of γ which permit a noise reduction (negative values) whilst the higher frequencies (5,10) give consistent noise increases for all values of γ. As the frequency is increased further (50), the variation with γ tends to zero simply because porosity is ineffective, thus varying it has little effect.

Figure 16 shows that when the leading edge is porous ($\alpha_L = 0.1$), the trend for all frequencies is that increasing γ increases noise in contrast to our previous result. This, however, is perhaps the simplest case to interpret first; each different value of γ describes a plate with a different average porosity ($0.5\int_{-1}^{1} \alpha_H(x)\,\mathrm{d}x$). The larger the value of γ, the

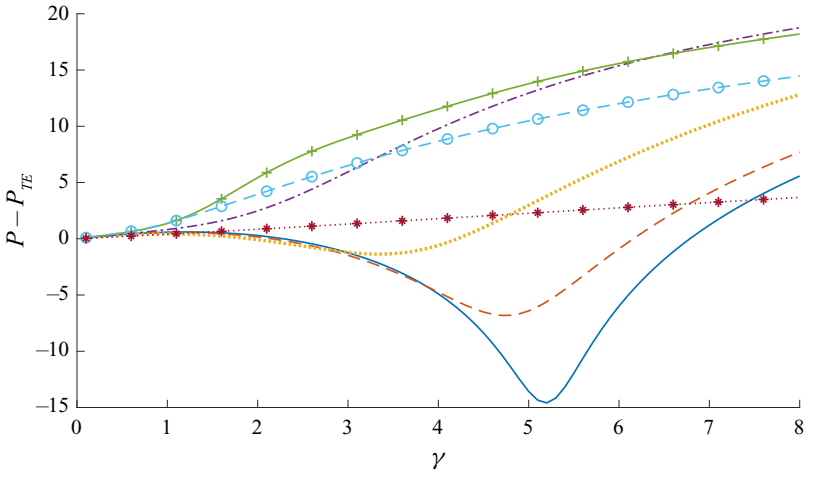

FIGURE 15. Effect of different monotonic variations of porosity from $\alpha_H = 0$ to 0.1 on trailing-edge noise. Legend is identical to that for figure 14.

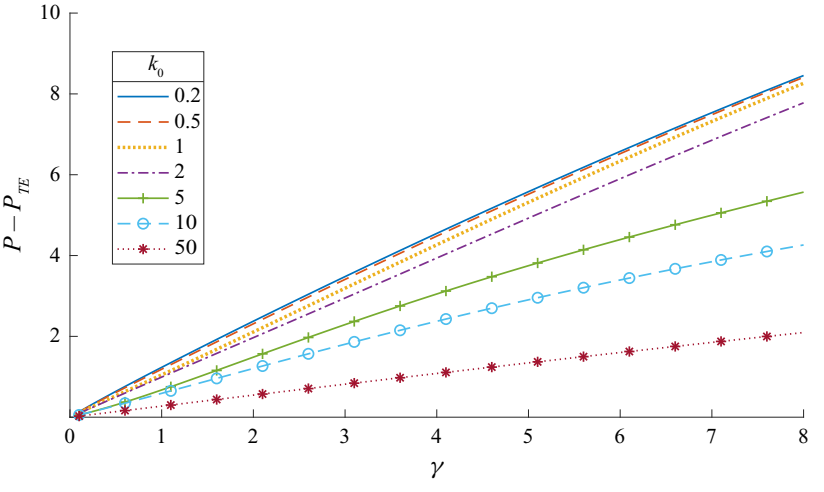

FIGURE 16. Effect of different monotonic variations of porosity from $\alpha_H = 0.1$ to 0.3 on trailing-edge noise.

lower the average porosity, particularly in the vicinity of the quadrupole at the trailing edge, thus the more noise will radiate from the interaction of the acoustic source with the plate on comparison to a plate with a constant, higher porosity, of α_T throughout.

This theory holds for the high-frequency cases in figures 14 and 15, however, at low frequencies, we see very different behaviour. The fact that the leading edge is specifically impermeable, $\alpha_L = 0$, must play a key role in the acoustic scattering, and peculiarly, by introducing a less porous region of the plate, we find values of γ at which the noise significantly reduces. We, therefore, consider the effect of varying the leading-edge porosity value, α_L, for fixed $\gamma = 2$ and fixed $\alpha_T = 0.3$ in figure 17. If $\alpha_L \neq 0$, the effect of increasing the porosity at the leading edge is to uniformly reduce the noise across all frequencies, due to the increasing average porosity of the total plate. However, specifically

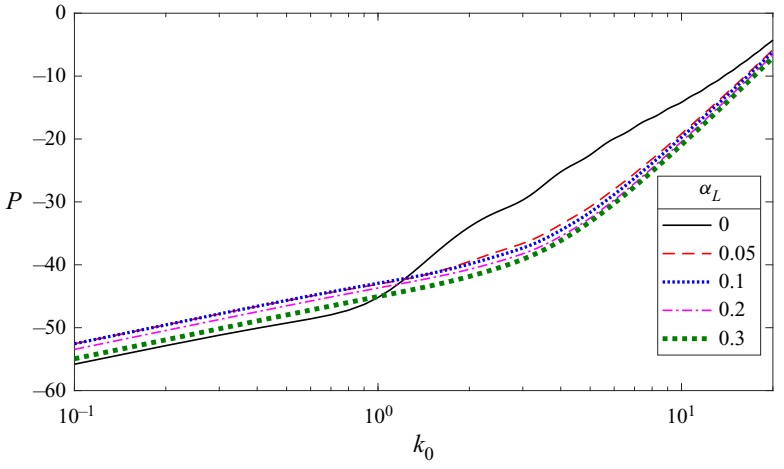

FIGURE 17. Effect of varying α_L on trailing-edge noise over a range of frequencies. In all cases the porosity at the trailing edge is fixed at $\alpha_T = 0.3$.

$\alpha_L = 0$ opposes this trend at low frequencies, where the noise is reduced versus even a plate with a constant higher porosity of $\alpha_T = 0.3$.

The fact that this trend alters at low frequencies where the plate is acoustically compact is not unexpected. For impermeable plates, back scattering from the leading edge (Moreau & Roger 2009) is a significant contributor to the total far-field noise. This back scattering arises because a non-zero jump in pressure across the plate at the leading edge must be smoothly reduced to zero upstream of the plate. If the leading edge is porous, $\alpha_L > 0$, the back scattering is much weaker than if $\alpha_L = 0$, since there is communication between the upper and lower surfaces of the plate and the pressure jump across the plate at the (porous) leading edge is dampened (Chaitanya *et al.* 2020). This gives rise to two possible reasons for noise reduction at low frequencies as we vary γ; increased average plate porosity and back scattering effects result in edge-to-edge interference.

Recently, Chaitanya *et al.* (2020) proposed source-cutoff and edge-to-edge interference as the two main noise-reduction mechanisms for fully and partially porous flat plates, when in the porous section the porosity is uniformly distributed. A possible alternative explanation for the source cutoff is due to the presence of evanescent surface waves of the form $\exp(\mathrm{i}\alpha k_0 x \pm \sqrt{1-\alpha^2}y)$ by the impedance-type boundary condition of the form $\mathrm{i}k_0 p = Z(\partial p/\partial y)$, as previously observed by Rienstra & Hirschberg (2004) (where $\alpha = \pm\sqrt{1-Z^{-2}}$). For our porous plate model, $Z = -\mathrm{i}\mu/k_0$ thus is purely imaginary, and these surface waves may be induced. For variable-porosity plates, any surface wave structure will be more complex and is not focussed on in this current study any further.

For our variable-porosity plate, in all cases of $\alpha_L > 0$ the back scattering and hence edge-to-edge interference may be neglected since the leading-edge porosity dampens the jump in surface pressure, and we hypothesise that the overall acoustic behaviour depends only on the relative average porosity, thus mimics the high-frequency behaviour. For a plate with an impermeable leading edge, the back scattering cannot be neglected, and thus generates an additional acoustic source at the leading edge. Depending on the relative source strength of these sources, at a given frequency when the two sources are out of phase they will destructively interfere to result in a lower total amount of far-field noise. Similarly, if the back scattering is in phase, additional noise will be created. We illustrate

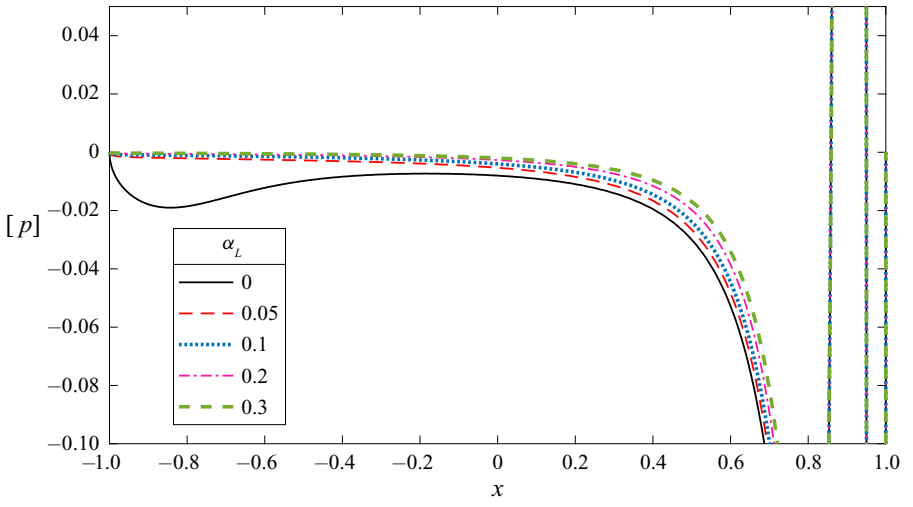

FIGURE 18. Effect of varying α_L on the jump in (real) surface pressure, $[p]$ for $k_0 = 0.5$. In all cases the porosity at the trailing edge is fixed at $\alpha_T = 0.3$, and $\gamma = 2$.

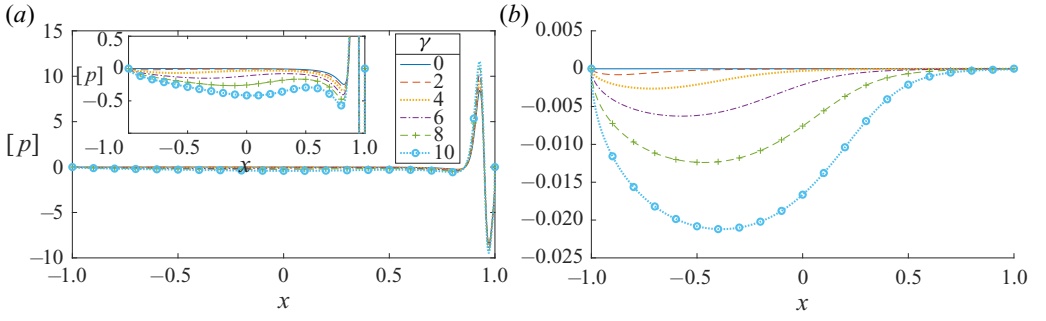

FIGURE 19. Effect of varying γ on the jump in surface pressure, $[p]$, for $k_0 = 0.5$. (a) Shows the real part of $[p]$, (b) the imaginary part. In all cases the porosity at the trailing edge is fixed at $\alpha_T = 0.3$, and at the leading edge at $\alpha_L = 0$.

this feature by considering the jump in surface pressure along the plate in figure 18. There is a clear pressure jump induced near the leading edge for $\alpha_L = 0$, which is not present for porous leading edges even when the porosity is very small.

We investigate the effect of γ on this pressure jump near the leading edge in figures 19 and 20 for low and high frequencies. Both real and imaginary parts of the pressure jump are now given. At low frequencies for small γ, the pressure jump near the leading edge is dominated by a negative real part. However, as γ increases the imaginary part near the leading edge increases. Therefore, the relative phase difference between the fields alters, and an optimal γ value should exist whereby the fields are in optimal destructive interference with each other. This is in contrast to the back scattering for a fully impermeable plate, whereby the respective pressure jump across the plate is always positive for low frequency $k_0 = 0.5$, as illustrated in figure 21, and only a fixed interference can be achieved. The ability of the variably porous plate to induce a destructively interfering leading-edge field is echoed by the minimum feature in figure 13, which illustrates a value of γ exists for which the total scattered noise is minimal.

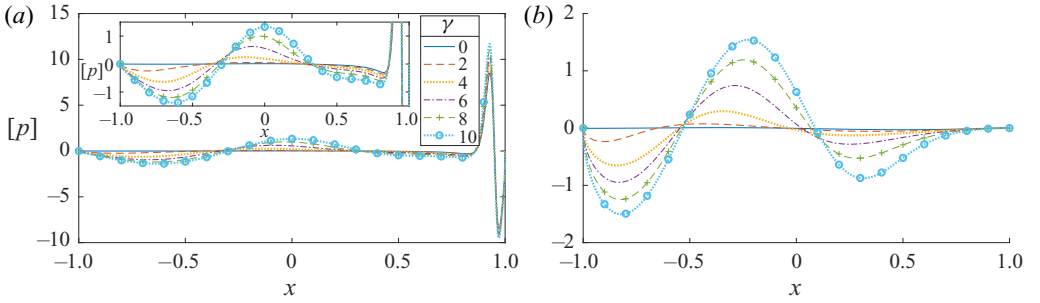

FIGURE 20. Effect of varying γ on the jump in surface pressure, $[p]$, for $k_0 = 5$. (a) Shows the real part of $[p]$, (b) the imaginary part. In all cases the porosity at the trailing edge is fixed at $\alpha_T = 0.3$, and at the leading edge at $\alpha_L = 0$.

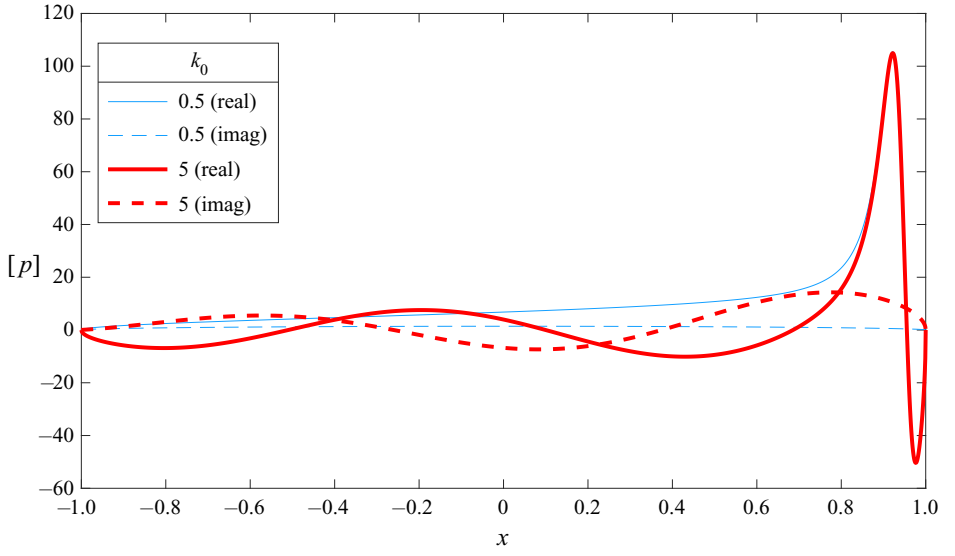

FIGURE 21. Jump in surface pressure, $[p]$, for $k_0 = 0.5, 5$ in the case of an impermeable plate, $\alpha_H = 0$.

At the higher frequency, $k_0 = 5$, the real and imaginary parts of $[p]$ in figures 19 and 20 are both oscillatory and similar in magnitude across all values of γ. This is very similar to the case for the impermeable plate in figure 21. We, therefore, expect that at high frequencies any back scattering effects for a variable porous plate with an impermeable leading edge are similar to those observed for a fully impermeable plate, namely that the magnitude of the back scattering is significantly reduced (Moreau & Roger 2009) and does not play a key role in the overall far-field noise.

Our results, therefore, corroborate the hypothesis that low-frequency behaviour is dominated by back scattering when the leading edge is rigid, and high-frequency behaviour is dominated by average plate porosity. This neglects the possibility of surface wave source cutoff, for which a more detail numerical study would be required to fully validate our hypothesis in case these surface waves may also play a role.

Finally, we consider the far-field directivities at different frequencies for various porosity distributions to again illustrate the hypothesised noise-reduction mechanisms. These two

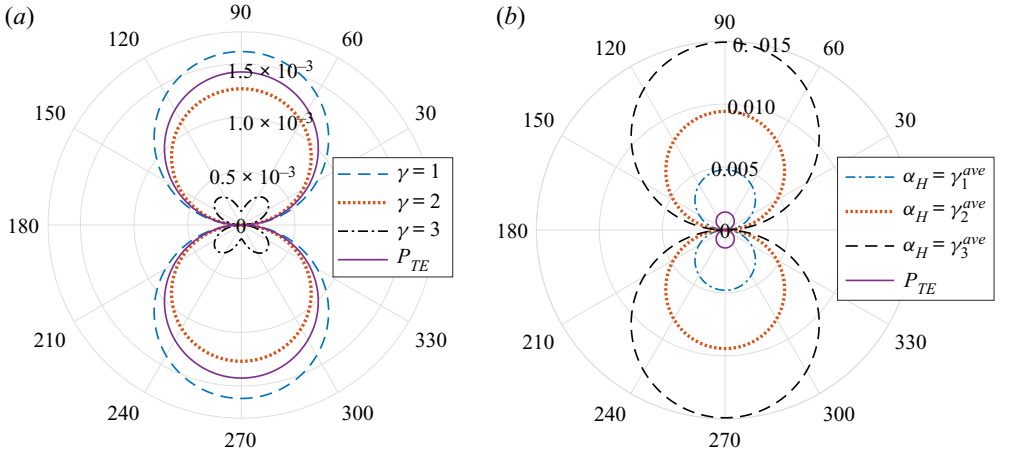

FIGURE 22. Directivity, $|D(\theta)|$, for a quadrupole near the trailing edge with $k_0 = 0.2$, when $\alpha_L = 0$ and $\alpha_T = 0.3$. P_{TE} denotes the directivity if $\alpha_H = \alpha_T$ throughout, and $\alpha_H = \gamma_i^{ave}$ denotes the directivity if α_H takes a constant value equal to the average porosity when $\gamma = i$.

mechanisms which operate as we alter the porosity distribution by varying γ are the change in average porosity, and the relative interference of the main trailing-edge acoustic field and the back scattered leading-edge field. Due to the importance of this back scattered field at low frequencies, the interference feature should overpower the effect of average plate porosity at values of γ where the two fields are out of phase. This is illustrated in figure 22; if we take a plate with constant porosity (right) and decrease that porosity, the far-field noise uniformly increases (recall $\alpha_{TE} > \gamma_1^{ave} > \gamma_2^{ave} > \gamma_3^{ave}$). However, if we take a plate and alter the porosity through the variable $\alpha_H(x)$ (left), we see completely different behaviour; now the noise may reduce even though average plate porosity has decreased (γ has increased). The reduction here is due to the tuned phase difference between the main trailing-edge field and the back scattered field. This cannot be achieved for a plate with constant porosity, since in that case an insufficiently strong back scattered field is generated.

In figure 23 we repeat the results from figure 22, but now change the leading-edge value of the variable porosity cases to $\alpha_L = 0.1$. The leading-edge back scattered field is now heavily reduced since the surface pressure jump is dampened, and correspondingly altering the value of γ results in an identical trend to altering the average porosity of the plate. The overall magnitudes of the directivities for constant or variable porosity differ since each variable-porosity case, $\gamma = 1, 2, 3$, has a higher porosity at the trailing edge than the average cases.

At higher frequencies, where the plate is non-compact, the overwhelming noise source becomes dominated by the trailing edge. The far-field acoustic behaviour, therefore, returns to a dependence on just average porosity of the plate, regardless of whether the leading edge of the variable plate has zero porosity or not. This can be seen in figure 24; the same increasing noise trend is seen as γ increases as when the average plate porosity decreases. This is true for both the zero-porosity leading edge and the non-zero-porosity leading edge. We note, however, the variation in the directivity shape between constant and variable-porosity cases when the leading-edge is impermeable (left). The directivity is more oscillatory when $\alpha_L = 0$ but not when the leading edge is porous. The oscillations in the impermeable leading-edge case are caused by the small, $O(k_0^{-1/2})$,

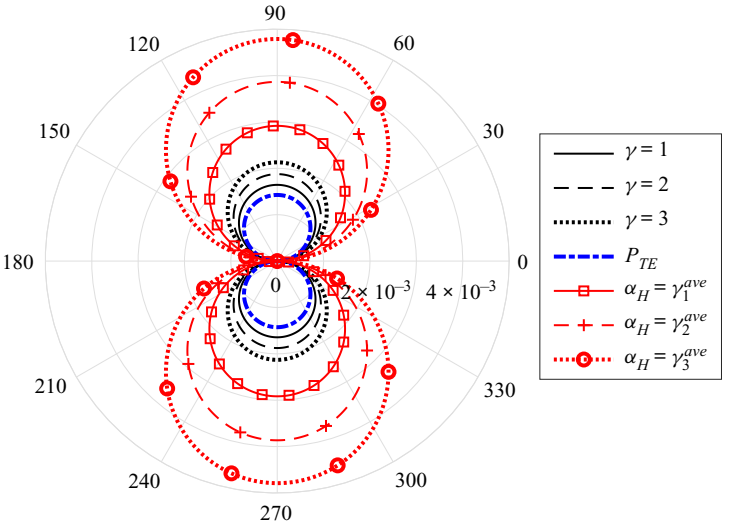

FIGURE 23. Directivity, $|D(\theta)|$, for a quadrupole near the trailing edge with $k_0 = 0.2$, when $\alpha_L = 0.1$ and $\alpha_T = 0.3$. P_{TE} denotes the directivity if $\alpha_H = \alpha_T$ throughout, and $\alpha_H = \gamma_i^{ave}$ denotes the directivity if α_H takes a constant value equal to the average porosity when $\gamma = i$.

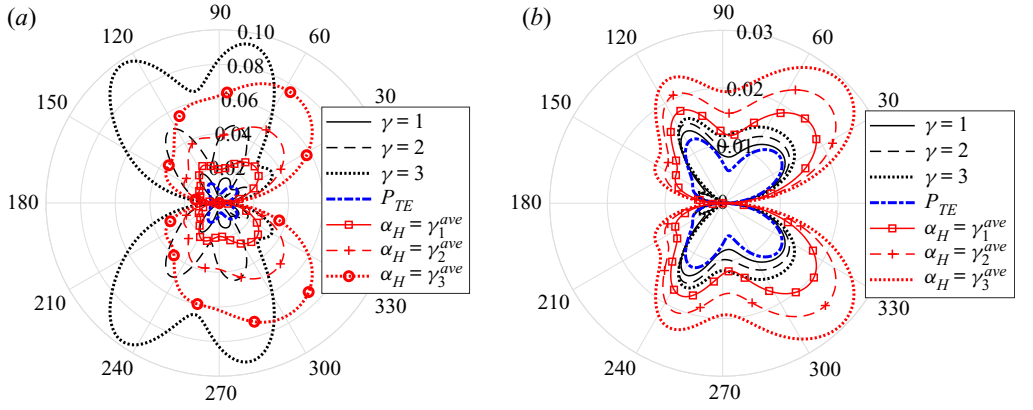

FIGURE 24. Directivity, $|D(\theta)|$, for a quadrupole near the trailing edge with $k_0 = 5$, when $\alpha_L = 0$ (*a*) and $\alpha_L = 0.1$ (*b*). For both, $\alpha_T = 0.3$, P_{TE} denotes the directivity if $\alpha_H = \alpha_T$ throughout, and $\alpha_H = \gamma_i^{ave}$ denotes the directivity if α_H takes a constant value equal to the average porosity when $\gamma = i$.

back scattering effects which are still present at high frequencies albeit are less crucial to the overall magnitude of the directivity. When the leading edge is porous, similar to at low frequencies, the back scattering is reduced, and the oscillations become much less pronounced.

6. Conclusions

This paper has considered the aeroacoustic effects of plates with chordwise-varying porosity distributions. We have measured the distributions from two species of bird; the barn owl and the common buzzard, and matched their chordwise-varying air flow

resistance to an effective open area ratio as arises in the acoustic theoretical modelling of perforated plates. A plate with a porosity mimicking that of the buzzard's is seen to be more aerodynamically efficient, whilst one modelling the owl's produces much less noise than the buzzard. The additional camber of the owl's wing, which is not included in the results here, may mitigate the adverse aerodynamic effects of porosity. The aeroacoustic effect of camber is known to be small (Devenport, Staubs & Glegg 2010), particularly in comparison to the effect of surface porosity. Therefore we would not expect including camber in our acoustic model to significantly alter those results. The noise reduction observed is in agreement with previous experimental results for uniformly porous plates, and is shown to be similar to that measured during flyover tests. However, the theory over-predicts that seen in laboratory tests. This is most likely due to additional features on the owl's wing that promote silent flight such as serrations and a downy upper coat. These features have not been modelled here.

A further study of the effects of general monotonic streamwise distributions was then undertaken. It is seen that for low frequencies, a monotonic variation from a porous trailing edge to an impermeable leading edge can be more acoustically beneficial than if the plate remained at the constant trailing-edge porosity. This is attributed to the leading-edge back scattered field (Moreau & Roger 2009); an impermeable leading edge has a strong back scattered field which is able to destructively interfere with the trailing-edge field. At high frequencies, the back scattered field is both weaker and of much higher frequency, therefore inducing oscillations in the far-field directivity rather than a global reduction (or increase) of noise.

This model cannot capture the effects of finite wing span or roughness-induced noise, both of which will affect the noise generated by a realistic wing. Nevertheless, we hope the theoretical acoustic model developed here, combined with a previous aerodynamic model (Hajian & Jaworski 2017), may be useful for future simultaneous studies of the effects of porosity on aerodynamic and aeroacoustic efficiency, and may aid in the design of new quiet aerofoils. The particular route of interest highlighted here is in varying the porosity of a plate in such a way as to induce a destructively interfering acoustic field. This has the potential to benefit both the acoustics and the aerodynamics.

Acknowledgements

The work here has been funded by EPSRC Early Career Fellowship EP/P015980/1 (L.J.A.), and EPSRC grant EP/L016516/1 (M.J.C.). P.C. would like to acknowledge the financial support of the Royal Academy of Engineering (RF/201819/18/194). The authors also acknowledge the help of C. Fritzsche, Thomas Windisch and T. Drescher with the acquisition of the wings and the air flow resistivity measurements as well as Dr M. Päckert and J. Ziegler of the Senckenberg Naturhistorische Sammlungen Dresden for the preparation of the wings. Finally, the authors thank the anonymous reviewers for their keen questions and suggestions that greatly enhanced this paper.

Declaration of interests

The authors report no conflict of interest.

REFERENCES

ALERSTAM, T., ROSÉN, M., BÄCKMAN, J., ERICSON, P. G. P. & HELLGREN, O. 2007 Flight speeds among bird species: allometric and phylogenetic effects. *PLOS Biol.* **5** (8), e197.

AYTON, L. J. 2016 Acoustic scattering by a finite rigid plate with a poroelastic extension. *J. Fluid Mech.* **791**, 414–438.

AYTON, L. J. & KIM, J. W. 2018 An analytic solution for the noise generated by gust–aerofoil interaction for plates with serrated leading edges. *J. Fluid Mech.* **853**, 515–536.

BACHMANN, T., KLÄN, S., BAUMGARTNER, W., KLASS, M., SCHRODER, W. & WAGNER, H. 2007 Morphometric characterisation of wing feathers of the barn owl *Tyto alba pratincola* and the pigeon *Columba livia*. *Front. Zool.* **4**, 23.

BACHMANN, T., MÜHLENBRUCH, G. & WAGNER, H. 2011 The barn owl wing: an inspiration for silent flight in the aviation industry? In *Bioinspiration, Biomimetics, and Bioreplication*, Proc. SPIE, vol. 7975, 79750N. International Society for Optics and Photonics.

BACHMANN, T., WAGNER, H. & TROPEA, C 2012 Inner vane fringes of barn owl feathers reconsidered: morphometric data and functional aspects. *J. Anat.* **221**, 1–8.

BAE, Y. & MOON, Y. J. 2011 Effect of passive porous surface on the trailing-edge noise. *Phys. Fluids* **23** (12), 126101.

BOYD, J. P. 2001 *Chebyshev and Fourier Spectral Methods*. Courier Corporation.

CAVALIERI, A. V. G., WOLF, W. R. & JAWORSKI, J. W. 2016 Numerical solution of acoustic scattering by finite perforated elastic plates. *Proc. R. Soc. A* **472**, 20150767.

CHAITANYA, P., JOSEPH, P., CHONG, T. Z., PRIDDIN, M. & AYTON, L. 2020 On the noise reduction mechanisms of porous aerofoil leading edges. *J. Sound Vib.* **485**, 115574.

CHEN, K., LIU, Q., LIAO, G., YANG, Y., REN, L., YANG, H. & CHEN, X. 2012 The sound suppression characteristics of wing feather of owl (*Bubo bubo*). *J. Bionic. Engng* **9** (2), 192–199.

COLBROOK, M. J. & PRIDDIN, M. J. 2020 Fast and spectrally accurate numerical methods for perforated screens (with applications to Robin boundary conditions). *IMA J. Appl. Maths* **85**, hxaa021.

DEVENPORT, W. J., STAUBS, J. K. & GLEGG, S. A. L. 2010 Sound radiation from real airfoils in turbulence. *J. Sound Vib.* **329** (17), 3470–3483.

DRISCOLL, T. A., HALE, N. & TREFETHEN, L. N. 2014 *Chebfun Guide*. Pafnuty Publications.

GEYER, T. F. & SARRADJ, E. 2014 Trailing edge noise of partially porous airfoils. In *20th AIAA/CEAS Aeroacoustics Conference Atlanta*, pp. 2014–3039. AIAA.

GEYER, T. F. & SARRADJ, E. 2019 Self noise reduction and aerodynamics of airfoils with porous trailing edges. In *Acoustics*, vol. 1, pp. 393–409. Multidisciplinary Digital Publishing Institute.

GEYER, T. F., SARRADJ, E. & FRITZSCHE, C 2010 Measurement of the noise generation at the trailing edge of porous airfoils. *Exp. Fluids* **48**, 291–308.

GEYER, T. F., SARRADJ, E. & FRITZSCHE, C. 2013 Silent owl flight: Comparative acoustic wind tunnel measurements on prepared wings. *Acta Acust. United Ac* **99** (1).

GEYER, T. F., SARRADJ, E. & GIESLER, J. 2012 Application of a beamforming technique to the measurement of airfoil leading edge noise. *Adv. Acoust. Vib.* **2012**.

GRAHAM, R. R. 1934 The silent flight of owls. *Aeronaut. J.* **38** (286), 837–843.

HAJIAN, R. & JAWORSKI, J. W. 2017 The steady aerodynamics of aerofoils with porosity gradients. *Proc. R. Soc. Lond.* A **473** (2205), 20170266.

HERR, M. 2007 Design criteria for low-noise trailing-edges. In *13th AIAA/CEAS Aeroacoustics Conference*, pp. 2007–3470. AIAA.

HOWE, M. S. 1998 *Acoustics of Fluid-Structure Interactions*. Cambridge University Press.

HOWE, M. S., SCOTT, M. I. & SIPCIC, S. R. 1996 The influence of tangential mean flow on the Rayleigh conductivity of an aperture. *Proc. Roy. Soc.* A **452** (1953), 2303–2317.

IOSILEVSKII, G. 2011 Aerodynamics of permeable membrane wings. *Eur. J. Mech.* B/*Fluids* **30** (5), 534–542.

ISO 9053 1991 Acoustics-materials for acoustical applications-determination of air-flow resistance.

JAWORSKI, J. W. & PEAKE, N. 2013 Aerodynamic noise from a poroelastic edge with implications for the silent flight of owls. *J. Fluid Mech.* **723**, 456–479.

JAWORSKI, J. W. & PEAKE, N. 2020 Aeroacoustics of silent owl flight. *Annu. Rev. Fluid Mech.* **52** (1), 395–420.

JONES, M. G., NARK, D. M., WATSON, W. R. & HOWERTON, B. M. 2017 Variable-depth liner evaluation using two NASA flow ducts. In *23rd AIAA/CEAS Aeroacoustics Conference*, pp. 2017–3022, https://arc.aiaa.org/doi/pdf/10.2514/6.2017-3022. AIAA.

LILLEY, G. 1998 A study of the silent flight of the owl. In *4th AIAA/CEAS Aeroacoustics Conference*, p. 2340. AIAA.

MCLACHLAN, N. W. 1964 *Theory and Application of Mathieu Functions*. Dover.

MOREAU, D. J. & DOOLAN, C. J. 2013 Noise-reduction mechanism of a flat-plate serrated trailing edge. *AIAA J.* **51** (10), 2513–2522.

MOREAU, S. & ROGER, M. 2009 Backscattering correction and further extensions of Amiet's trailing-edge noise model. Part II: application. *J. Sound Vib.* **323**, 397–425.

NACHTIGALL, W. & KLIMBINGAT, A 1985 Messung der Flügelgeometrie mit der Profilkamm-Methode und geometrische Flügelkennzeichnung einheimischer Eulen. *Biona-report* **3**, 45–86.

NEUHAUS, W., BRETTING, H. & SCHWEIZER, B. 1973 Morphologische und funktionelle Untersuchungen über den 'lautlosen' Flug der Eulen (*Strix aluco*) im Vergleich zum Flug der Enten (*Anas platyrhynchos*). *Biol. Zbl.* **92**, 495–512.

OLVER, F. W. J., LOZIER, D. W., BOISVERT, R. F. & CLARK, C. W. 2010 *NIST Handbook of Mathematical Functions*. Cambridge University Press.

RAYLEIGH, LORD 1945 *The Theory of Sound*, vol. 2. Dover.

RIENSTRA, S. & HIRSCHBERG, A. 2004 *An Introduction to Acoustics*. Eindhoven University of Technology.

RIENSTRA, S. & PEAKE, N. 2005 Modal scattering at an impedance transition in a lined flow duct. In *11th AIAA/CEAS Aeroacoustics Conference*, pp. 2005–2852. AIAA

ROGER, M., SCHRAM, C. & DE SANTANA, L. 2013 Reduction of airfoil turbulence-impingement noise by means of leading-edge serrations and/or porous material. In *19th AIAA/CEAS Aeroacoustics Conference*, p. 2108. AIAA

SARRADJ, E., FRITZSCHE, C. & GEYER, T. F. 2010 Silent owl flight: bird flyover noise measurements. In *16th AIAA/CEAS Aeroacoustics Conference*, pp. 2010–3991.

TREFETHEN, L. N. 2000 *Spectral Methods in MATLAB*, vol. 10. SIAM.

TSAI, C.-T. 1992 Effect of airfoil thickness on high-frequency gust interaction noise. PhD thesis, University of Arizona.